Galactic Outflows in Starburst Dwarf Galaxies Detected in Diffuse X-ray Emission

A THESIS
SUBMITTED TO THE FACULTY OF THE GRADUATE SCHOOL
OF THE UNIVERSITY OF MINNESOTA
BY

Heilman, Taryn N.

IN PARTIAL FULFILLMENT OF THE REQUIREMENTS
FOR THE DEGREE OF
MASTER OF SCIENCE

Skillman, Evan D.

December, 2015

Acknowledgements

I'd like to extend my gratitude to all the people that have helped me in graduate school. First and foremost to Kristen McQuinn and Evan Skillman for all of the advice and support throughout this project. I'd also like to thank the entire MiFA faculty, especially my committee members, and my fellow grad students, without whom I would not have survived this long.

This research has made use of "Aladin sky atlas" developed at CDS, Strasbourg Observatory, France (Boch & Fernique, 2014; Bonnarel et al., 2000) This research has made use of the NASA/IPAC Extragalactic Database (NED), which is operated by the Jet Propulsion Laboratory, California Institute of Technology, under contract with the National Aeronautics and Space Administration. I acknowledge the usage of the HyperLeda database (http://leda.univ-lyon1.fr) This work made use of the *ACIS Extract*(AE) software package (Broos et al., 2010, 2012).

Dedication

To Sarah, who has always inspired me, and to Tom, who has been my rock since day two of graduate school.

Abstract

We present an analysis of archival Chandra X-ray observations of a sample of six nearby dwarf starburst galaxies (DDO 165, NGC 625, NGC 1569, NGC 4214, NGC 4449, NGC 5253). This work presents maps of diffuse X-ray emission with point sources removed. We find evidence of diffuse X-ray emission extended beyond the optical disc in four of six galaxies in the sample. The diffuse emission is best fit to single or two temperature thermal plasma models with temperatures of 0.14-0.8 keV. In galaxies with extended emission detected, emission extends up to 5 kpc from the nuclei of the galaxies, and all show unique morphologies. We compare X-ray data to ancillary UV and optical data from the STARBIRDS project and archival radio wavelengths. Diffuse X-ray emission generally corresponds with star forming regions emitting in the Near UV, and/or with an under-density in the H I disc. Our analysis shows that diffuse X-ray emission is strongly correlated with star formation on both short ($\sim$10 Myr) and long timescales (200-400 Myrs). The shorter timescales agree with previous studies, however the agreement on long timescales suggest the picture is more complex. Our analysis combined with star formation histories conflict with previous works assuming $\sim$10 Myr burst timescales and constant star formation rates, suggesting that longer, time-varying star formation rates are essential to truly understanding stellar feedback and galactic winds.

Contents

List of Tables

List of Figures

Chapter 1

Introduction

- Chapter 1, this page, outlines the structure of the body of this work.
- Chapter 2 briefly presents the background science of starbursting dwarf galaxies, stellar feedback and X-ray emission, and the goals of this work.
- In Chapter 3, the X-ray observations as well as ancillary data used for the galaxy sample and STARBIRDS project are described in detail.
- Chapter 4 describes the steps taken to clean and reduce X-ray data, remove point sources, and flux calibrate the diffuse emission.
- Chapter 5 compares the luminosity and morphology of diffuse X-ray emission with temporal information from the optical catalogs of the resolved stellar populations, and the X-ray flux is compared with UV, optical and radio imaging of the sample.
- Chapter 6 presents our conclusions.

Chapter 2

Science

Starbursts are short-lived periods of intense star formation that are unsustainable over a Hubble time, based on gas consumption timescale arguments (Searle et al., 1973). Starburst events have been measured to have durations of a few 100 Myr and typically last as long or longer than the dynamical time scales of the host galaxy (McQuinn et al., 2009, 2010b). Those studies showed that starbursts last at least an order of magnitude longer than the 5-10 Myr often reported (e.g., Schaerer et al., 1999; Mas-Hesse & Kunth, 1999). The spatial extent of the bursts can vary from centralized to extending over significant fractions of the optical disk (McQuinn et al., 2012). The longer-lasting and more spatially distributed bursts can have a correspondingly larger impact on the evolution of the dynamics, chemical evolution, and future star formation of the host galaxy.

Massive young stars formed in starburst events have strong stellar winds and eventually explode as Type II supernovae, heating the interstellar medium (ISM), causing bubbles and superbubbles of heated, metal enriched, low density gas. Dwarf galaxies are observed to be ideal environments for the growth of these superbubbles, due to their nearly solid body rotation and subsolar metallicities (Martin, 1998). Simulations show that superbubbles can expand far enough to "blow out" of the galactic disk (Mac Low & McCray, 1988), preferentially along the minor axis. Dwarf galaxies are expected to experience the most drastic consequences from these blowouts due to their shallow potential wells.

Outflows and winds from dwarf galaxies have several important implications. First,

closed box chemical evolution models often over-predict the metallicity in dwarf galaxies (Matteucci & Chiosi, 1983). Galactic winds are often invoked to explain the expulsion of metal-enriched material from the galaxy (e.g., Mac Low & Ferrara, 1999; Martin et al., 2002), as well as enrichment of the IGM, Cen & Chisari (e.g., 2011). The IGM is a hot ($10^5 - 10^7$ K), rarefied gas that occupies the space between galaxies, and is thought to contain 40-50% of the baryons in the universe (Bykov et al., 2008). Pollution of the IGM with heavy elements can have significant ramifications, especially in the early universe. A further implication is that strong galactic winds may eject enough of the ISM from the galaxy to shut off star formation completely (De Young & Heckman, 1994). In the early universe, starbursts were more common as more gas was present within galaxies to fuel starburst activity and there was a higher frequency of burst-triggering gravitational interactions and mergers. Therefore, starburst driven winds may be important cosmologically, as dwarf galaxies formed rapidly, underwent starburst events, polluted the IGM, and formed the building blocks of large spirals. Starburst dwarf galaxies in the local universe are a valuable tool to study this powerful phenomenon in detail, both as proxies for galactic evolution in the early universe and as a source of insight as to how starbursts affect their local environments.

Galactic outflows have been identified in several well studied systems, (e.g. NGC 253, NGC 1569; Martin et al., 2002; Strickland et al., 2000). However, there is not conclusive evidence that outflows are ubiquitous in low-mass galaxies, or enough data to robustly quantify the role of winds in galaxy and IGM evolution (Skillman, 1997). This work explores six nearby dwarfs undergoing starbursts, using archival Chandra data. In these energetic galaxies, we expect to find evidence of hot coronal gas visible as diffuse, soft X-ray emission that is ideal for looking for galactic outflows. Compact X-ray point sources, such as background active galactic nuclei and X-ray binary systems, emit hard X-rays in a non-thermal regime. These point sources, which can complicate identification of diffuse X-ray emission, were removed, leaving the soft X-rays generated by thermal processes such as Bremsstrahlung radiation. The diffuse emission allows us to examine the morphology of this hot gas to look for galactic winds, outflows, and other structure in the ISM.

Many papers (e.g., Martin et al., 2002; Summers et al., 2003, 2004; Hartwell et al., 2004) have imparted valuable knowledge about the X-ray emission of individual systems,

however, our uniform analysis of X-ray emission and detailed star formation histories (SFHs) allow us to examine the relationship between star formation rates (SFRs) and X-ray luminosity, and explore the frequency of starburst driven outflows. We describe the morphology and quantify diffuse X-ray emission, look for correlations with SFRs and emission at other wavelengths, and examine timescales associated with star formation feedback and galactic winds.

Chapter 3

The Galaxy Sample and Observations

The six galaxies in this sample are a subset of the panchromatic STARBurst IRregular Dwarf Survey (STARBIRDS, McQuinn et al., 2015), a survey of 18 starburst dwarf irregular galaxies in the nearby ($D < 6$ Mpc) universe. The 6 galaxies were selected based on the availability of Chandra archival data with fields of view overlapping with HST observations used in previous works (McQuinn et al., 2010a,b, 2012). The basic properties of this sample and the X-ray observations are described in Table 3.1.

The STARBIRDS sample galaxies exhibit ongoing starbursts, or show evidence of "fossil bursts". Local starburst environments afford a unique opportunity to study the effect that a starburst has on the evolution of the galaxy and the local universe. The 18 galaxies of the STARBIRDS sample were selected due to their Hubble Space Telescope (HST) photometry, reaching at least 2 magnitudes below the tip of the red giant branch (TRGB) in V and I bands, as well as their close proximity. The depth of the photometry ensures that the recent star formation can be accurately constrained (McQuinn et al., 2010a; Dolphin, 2002), and the proximity of the galaxies ensured that individual stars could be resolved. These properties allowed for robust reconstruction of the SFHs and measurements of durations (McQuinn et al., 2010b).

We compare the X-ray observations of these galaxies with observations at other wavelengths to investigate correlations between the morphology of X-ray emission and

spatial and temporal SFHs. Diffuse X-ray emission was analyzed and compared to data from optical catalogs (McQuinn et al., 2010a,b), UV emission (McQuinn et al., 2015), and neutral hydrogen maps (Lelli et al., 2014; Cannon et al., 2011).

3.1 X-ray Observations

Table 3.1 lists the X-ray observations of the galaxies in this sample. For our analysis, only data from the ACIS-S3 CCD detector were used. This detector has a high quantum efficiency (0.8 at 1 keV), high spectral resolution (120 eV), and high angular resolution (1 arcsec Garmire et al., 2003). The S3 chip is back-illuminated, which offers a better response at lower energies, making it ideal for studying diffuse emission.

Multiple observation campaigns per galaxy were available with overlapping, non-identical fields of view (FOVs). Observations were selected for best possible alignment with the previous HST observations. For galaxies with multiple epochs, data were reduced individually by epoch, and then reprojected and combined for analysis. Combining multiple observing epochs gave us a larger exposure time, greater than 100 ks in the cases of NGC 1569, NGC 4449 and NGC 5253. This increased our signal to noise (S/N), enabling us to detect extended emission at a high confidence level.

Previous works using these observations have analyzed diffuse X-ray emission and morphology for four of these galaxies, including Martin et al. (NGC 1569, obs 782 2002); Ott et al. (NGC 1569, obs 782 2005), Hartwell et al. (NGC 4214, obs 2030 2004); Ott et al. (NGC 4214, obs 2030 2005), Summers et al. (NGC 4449, obs 2031 2003); Ott et al. (NGC 4449, obs 2031 2005), and Summers et al. (NGC 5253, obs 2032 2004); Ott et al. (NGC 5253, obs 2032 2005). In each of these works, point sources were masked and the diffuse X-rays were fit to spectra and X-ray luminosity calculated. Our results will be compared to these in section 4.3. Martin et al. (2002); Hartwell et al. (2004); Summers et al. (2004) conclude from kinematic analysis that the hot coronal gas of NGC 1569, NGC 4214, and NGC 5253 may all have enough energy to escape the galaxies, while Summers et al. (2003) suggests that kinematic evidence for gas blowout is less conclusive due to a large H I halo. Ott et al. (2005) also complete kinematic analysis and find that NGC 1569 and NGC 4449 are energetic enough to have gas escape their halos, while NGC 4214 and NGC 5253 are not.

3.2 Ancillary Data

We use optical stellar catalogs and SFHs from McQuinn et al. (2010a), and derived from Advanced Camera for Surveys (ACS, Ford et al., 1998) and Wide Field Planetary Camera 2 (WFPC2, Holtzman et al., 1995) imaging with the F814W and either the F555W or F606W filters. SFHs were measured using the numerical CMD fitting technique `MATCH` (Dolphin, 2002) and the Padova stellar evolution models (Marigo et al., 2008). Briefly, `MATCH` uses a prescribed initial mass function (IMF) and stellar evolutionary isochrones to create a series of synthetic simple stellar populations (SSPs) of different ages and metallicities. The synthetic SSPs are modeled using the photometry and recovered fractions of the artificial stars as primary inputs. The modeled CMD that best-fits the observed CMD based on a Poisson likelihood statistic provides the most likely SFH of the galaxy. The SFH solutions were based on a Salpeter IMF (Salpeter, 1955), and an assumed binary fraction of 35% with a flat secondary distribution. The temporal resolution of the SFHs at recent times (t<500 Myr) allows us to compare the X-ray emission to the stellar mass formed over different epochs in each galaxy. This method is described in more detail in McQuinn et al. (2010a, and references therein). The catalogs of SFRs are used to look for temporal SFH correlations with the diffuse X-ray emission. This analysis is described in section 5.2.

We used GALEX FUV (1350-1750 Å) and NUV (1750-2250 Å) images from McQuinn et al. (2015), with fluxes and attenuation re-calculated to encompass the entire star forming disk of the galaxy. Attenuation at UV wavelengths were calculated from mid-infrared fluxes using the method detailed in Buat et al. (2005); McQuinn et al. (2015). The infrared images are archival MIPS data (Rieke et al., 2004) at the 24, 70, and 160 μm bands, obtained originally as part of the Local Volume Legacy Survey (LVL) (Dale at al., 2009) or the Spitzer Infrared Nearby Galaxy Survey (SINGS) (Kennicut et al., 2003; Regan & SINGS Team, 2004). NGC 1569 was not observed in either of those surveys, and so for this galaxy, we used the images available from the Spitzer Heritage Archive (SHA), which only covered 2 of the 3 MIPS bandpasses. Thus, for this galaxy, we could only calculate a lower limit for UV flux. The UV data are analyzed in greater detail in section 5.3.

Radio data used in this analysis are 21 cm H I moment 0 maps. For 5 of the 6

galaxies (NGC 625, NGC 1569, NGC 4214, NGC 4449, NGC 5253), the data cubes are from Lelli et al. (2014). The data cubes were blanked below 3σ and integrated over all velocity channels to produce to moment 0 maps using AIPS software. The DDO 165 moment 0 map was obtained from Cannon et al. (2011). The radio data are compared to the X-ray in section 5.1.

In addition to the NUV and radio images, we also overlaid X-ray contours on R-band optical images to compare morphologies. Optical images for DDO 165, NGC 4214, and NGC 4449 are taken from the SDSS DR12 (Alam et. al, 2015), while NGC 625, NGC 1569, and NGC 5253 are from the DSS 2 survey, obtained using the Aladin sky atlas database (Boch & Fernique, 2014; Bonnarel et al., 2000). These comparisons are discussed in section 5.1.

Table 3.1 Properties of the galaxy sample and archival X-ray observations

Galaxy	RA (J2000)	DEC	M_B (mag)	Distance (Mpc)	A_V (mag)	PI	Observation Number	Exposure Time (ksec)
DDO 165	13:06:24.85	+67:42:25.0	12.92	4.810	0.065	Jenkins	9537	13.72
							10868	10.72
NGC 625	01:35:04.63	-41:26:10.3	11.65	4.210	0.045	Skillman	4746	61.13
NGC 1569	04:30:49.06	+64:50:52.60	11.72	3.360	1.903	Martin	782	98.0
						Zezas	4745	10.15
NGC 4214	12:15:39.17	+36:19:36.8	10.21	2.950	0.06	Zezas	4743	27.56
							5197	28.96
						Heckman	2030	26.76
NGC 4449	12:28:11.10	+44:05:37.07	9.50	4.310	0.053	Long	10125	15.14
							10875	60.15
						Heckman	2031	26.94
NGC 5253	13:39:55.96	-31:38:24.38	10.80	3.560	0.153	Zezas	7153	69.12
							7154	67.49
						Heckman	2032	57.36

The summary of observations for the six galaxies used in this project. The right ascention (RA) and declination (DEC are in the Equatorial J2000 frame. A_v are calcuated from galactic column densities given by the Schlafly & Finkbeiner (2011) recalibration of the Schlegel et al. (1998) infrared based dust map, assuming a Fitzpatrick (1999) reddening law. Distances are TRGB distances taken from the NED database, from Grocholski et al. (2008) (NGC 1569), Mould & Sakai (2008) (NGC 5253), and Jacobs et al. (2009) (remaining).

Chapter 4

X-ray Data Reduction

The primary data set from Chandra, an events file, consists of photon counts in 4 dimensions: two spatial dimensions, time, and energy. X-ray detectors detect individual, sparse photons in events obeying Poisson statistics. Data reduction was carried out using CIAO version 4.7 and *ACIS Extract* (AE, Broos et al., 2010, 2012) following the methodology detailed in Tüllmann et al. (2011) and Binder et al. (2012), and followed three main stages. First, events files for each epoch were separated into three energy bands, deflared, and background subtracted. Second, point sources were identified, analyzed, and subtracted for each observation. Finally, flux maps were made for each observation, and then diffuse flux images were combined for analysis.

4.1 Pre-Processing and Image Cleaning

Data reprocessing was done using the *chandra_repro* tool, which updated the original events file with recalibrations, identified bad pixels, and constructed aspect solution files describing the orientation of the telescope as a function of time for each observation.

The X-ray data were divided into soft, medium, and hard energy bands both for analysis and the production of three-color images. Energy bands were chosen uniformly for all observations for a consistency to be 0.35-1 keV (soft), 1-2 keV (medium), and 2-7 keV (hard). We chose a wider soft band than other similar X-ray studies (e.g., Martin et al., 2002; Ott et al., 2005) to increase S/N in the soft band, where the diffuse, coronal emission is concentrated.

Flares are time intervals with unusually high count rates, caused by cosmic rays and their afterglows. Flares from cosmic rays can also lead to oversaturation of pixels on the detectors of *Chandra*. Some extraneous sources will result in a circle of excess detection around a center of oversaturated pixels with low counts and varying afterglow effects (CXC, private communication). Therefore, data were filtered to remove time intervals of both higher and lower than average count rates. This was done iteratively using the tool *lc_sigma_clip* with a 3σ inclusion criteria. Cosmic ray afterglows may last several dozen frames, so time bins were selected to be 144s, 45 times the intrinsic bin size of 3.2 s, to exclude the decaying tails of the afterglows. The stringent inclusion criterion increased confidence that our data are clean, which was more important for our science goals than small losses of good exposure time caused by the larger time bins.

Background subtraction was performed using the background event data set from the Chandra X-ray Center (CXC). The background event files were normalized for exposure time and subtracted from the primary image files. To ensure that the provided blank sky files were appropriate, we compared the statistics from the blank sky image files to a visually-selected empty patch of sky in each events file. Both the full and soft bands were compared, and in each case the standard deviation was several times larger than the mean, so differences were statistically consistent with zero. The blank sky files from the full energy band contained an average of $(7 \pm 22)\%$ fewer counts than our empty sky regions for the sample, and an average of $(3 \pm 28)\%$ fewer counts for the soft band.

4.2 Point Source Identification and Subtraction

Background subtracted event images were analyzed to identify and remove compact X-ray point sources such as AGN and X-ray binary star systems, leaving only diffuse emission behind. Removing these sources enables clean contours of the X-ray morphology, as well as better modeling of the emission in the flux calibration and subsequent luminosity calculation, detailed in section 4.3.

The source identification procedure was separated into two parts. The point sources were first located using *wavdetect* tool from CIAO, merged into one list per galaxy, and then analysed and filtered with Acis Extract (AE). After sources were identified and analyzed, they were removed from the images using tools in CIAO.

To identify possible point sources, we utilized the CIAO tool *wavdetect*, which correlates adjacent pixels using "Mexican Hat" wavelet functions with different scale sizes, and then searches the image for significant correlations. In order to ensure the identification of all real sources, a conservative significance threshold value of 10^{-4} was used. The significance threshold, or *sigthresh*, is the Poisson threshold for identifying a pixel as part of a source. Such a low threshold also identifies a number of false sources ($\sim$100 per megapixel), which will be removed after more careful analysis in AE. Furthermore, as many of the observations have overlapping fields of view, many of the point-source candidates within the source lists are duplicates. Source lists from *wavdetect* were merged by time bin, energy band, and epoch to create one source list for each galaxy.

This list of possible point sources was input to AE, which measures flux and assigns a probability no source (pns) value for each source. The pns value is the Poisson probability that all of the counts within the extraction region are background noise. Point source analysis was run on each observation separately, and the final source properties were assembled for each galaxy. We then iteratively filtered sources by their pns value, beginning with a value of 10^{-2}. All sources with pns above this value were rejected, and the rejected sources were visually inspected to make sure that no obvious sources had been removed. Any obvious point sources that were rejected were added back to the filtered source list. This list was passed through AE again for reanalysis, and the procedure iterated through pns values of 10^{-3}, 10^{-4}, and finally $4\text{x}10^{-6}$ (4.5σ detection). After the final filtration was completed, AE was run once again on the final source list to obtain the final regions and source properties. Initial and final numbers of point sources identified in each galaxy are shown in Table 4.1.

The final run of AE produced a region file defining irregular polygons that nominally enclose 90% of the source PSF, but may contain less counts to prevent overlapping in crowded regions. Using these regions as a guide, each point source was fit by eye an ellipse. The CIAO tools *roi* and *split roi* were then used to create regions enclosing the source and a background annulus based on these ellipses. The point source regions in the images were masked with pixel values interpolated from the surrounding background annuli to create maps of diffuse emission.

Diffuse emission maps were smoothed using the *csmooth* tool, which adaptively smoothes using a fast fourier transform algorithm that preserves the total number of

counts in each image. Smoothing was done using a circular Gaussian kernel of varying scale, increased until the total number of counts under the kernel exceeded the expected number of background counts in the kernel area. Diffuse maps were inspected by eye to ensure that subtracted regions were large enough to fully remove point sources, and not so large as to cause morphological changes. Figures 4.1 & 4.2 show smoothed X-ray emission in soft (red), medium (green), and hard (blue) bands with point sources, and then with the point-sources removed. Contour lines from the diffuse emission were used to define the boundary of emission associated with the galaxies for spectral extraction, and are used to examine morphology in section 5.1.

Table 4.1 Initial and final counts of X-ray point sources in combined observational epochs

Galaxy	Initially Detected	Final Sources
DDO 165	118	15
NGC 625	141	25
NGC 1569	937	50
NGC 4214	353	40
NGC 4449	1024	42
NGC 5253	1445	51

Initial number of point sources detected by wavdetect and final number of bona fide sources confirmed using ACIS Extract.

4.3 Flux calibration

To create flux images of the diffuse emission, we first needed to create instrument and exposure maps for each epoch. An instrument map accounts for the quantum efficiency of the detectors, as well as spatial non-uniformities of the detector array, mirror vignetting, and bad pixels. The exposure map is the product of the instrument map and the aspect histogram, which gives the time observed for each part of the sky. Detector effective area is highly energy dependent, therefore we needed to input a weighted spectral model into the instrument map to accurately calibrate the flux.

To create the weighted spectral models, we first extracted spectra from background subtracted, point source masked events files inside the region defined by the outermost

(2σ) contour line of emission associated with the galaxy from the diffuse counts images. Spectral models of the emission were computed in *sherpa* (Freeman et al., 2001) using two different spectral models: APEC plasma, *xsapec* (Astrophysical Plasma Emission Code, Smith et al., 2001; Raymond & Smith, 1977), and mekal plasma, *xsmekal* (after MEwe, KAastra & Liedahl, Mewe et al., 1995). Each of these emitting models consisted of a one or two temperature plasma, each component with an intrinsic absorbing component with variable metal abundances, as well as a foreground absorbing column. The internal extinction component was computed using the sherpa model *xsvphabs*, which is photoelectric absorption with variable metal abundances, with oxygen abundance given by McQuinn et al. (2015, and references therein), relative to a solar abundance of $12 + \log(O/H) = 8.69$ (Asplund et al., 2009). Foreground extinction was accounted for using the sherpa model *xsphabs*, simple photoelectric absorption, with Galactic column densities given by the Schlafly & Finkbeiner (2011) recalibration of the Schlegel et al. (1998) infrared based dust map. Parameters used in the models are detailed in Table 4.2.

Fitted spectral parameters are given in Table 4.3. NGC 625, NGC 4214, and NGC 4449 were best fit to single temperature plasmas of approximately 0.6, 0.3, and 0.3 keV, respectively. Temperatures for NGC 4214 and NGC 4449 agree with analysis by Ott et al. (2005). NGC 1569 and NGC 5253 were better fit to two temperature plasmas, with approximate components 0.65 and 0.24 keV (agreeing with Martin et al., 2002; Ott et al., 2005), and 0.7 and 0.2 keV (similar to Summers et al., 2004), respectively.

The spectral model outputs were averaged for each galaxy, and input into a spectral weight file to create weighted instrument maps, which give the effective area of the telescope mirror projected onto the detector surface with the detector quantum efficiency (QE), as a function of photon energy. The instrument maps are then convolved with the aspect histogram for the observation to give the exposure map, which has units of cm^2 sec counts photon^{-1}. Flux calibrated, extinction corrected images were made by dividing the filtered, background subtracted, diffuse counts images, with units of counts pixel^{-1} by the exposure map, to yield a surface brightness image, with units of photons cm^{-2} s^{-1} pixel^{-1}.

The final flux-calibrated images for each epoch were reprojected using the *reproject_image_grid* tool. This reprojects each fits file onto a custom grid large enough to encompass the fields of view of the multiple observing campaigns. Once the observations

were on identical grids, the images were averaged by pixel to create surface brightness maps for each galaxy. Images were summed inside the spectral extraction region to get the source flux, which is first converted to an energy flux by multiplying the broad band source flux by the expectation value of photon energy for that band, then converted to X-ray luminosity by multiplying by $4\pi D^2$, with distances as defined in Table 3.1. Source flux, energy flux, and luminosity values obtained for each galaxy using the two plasma models can be found in Table 4.4. Values varied a little between the two models but were consistent within 10-20%. For simplicity, only flux values from the mekal model were used for further analysis in Section 5, as this model is most commonly preferred in the literature (e.g., Ott et al., 2005; Hartwell et al., 2004). After accounting for choices of energy bands, values obtained for luminosities match those available in the literature for NGC 4449, NGC 5253, and NGC 4214 (Summers et al., 2003, 2004; Hartwell et al., 2004, respectively).

Table 4.2 Fixed parameters used in X-ray spectral fitting

Galaxy	Z (solar)	N_H (foreground)	z (redshift)
NGC 625	0.257	0.0084	0.001321
NGC 1569	0.316	0.36	-0.000347
NGC 4214	0.490	0.011	0.000970
NGC 4449	0.427	0.0099	0.000690
NGC 5253	0.257	0.029	0.001358

Parameters used in X-ray spectral fitting and flux calibration. (1) Metal abundances relative to solar defined by Asplund et al. (2009), with abundances determined from 12+log(O/H) listed in McQuinn et al. (2015, and references therein). (2) Galactic foreground hydrogen column density, in units of 10^{22} cm^{-2}, from Schlegel et al. (1998), using the relationship for N_H/A_V from Schnee et al. (2006). (3) Redshifts for galaxies, taken from NED database, from Huchtmeier et al. (2003, DDO 165), Koribalski et al. (2004, NGC625, NGC5253), Schneider et al. (1992, NGC 1569, NGC 4449) and de Vaucouleurs et al. (1991, NGC 4214).

Table 4.3 Fitted parameters from X-ray spectral fitting

Galaxy	Model	kT_1 (keV)	$norm_1$ (cm^{-5})	$N_{H,1}$ (cm^{-2})	kT_2 (keV)	$norm_2$ (cm^{-5})	$N_{H,1}$ (cm^{-2})
NGC 625	apec	0.66	6.1×10^{-6}	0.013	–	–	–
	mekal	0.56	1×10^{-6}	0.011	–	–	–
NGC 1569	apec	0.63	9.9×10^{-4}	0.55	0.22	1.5×10^{-3}	0.067
	mekal	0.67	9.4×10^{-4}	0.89	0.25	1.5×10^{-3}	0.065
NGC 4214	apec	0.28	1×10^{-6}	0.029	–	–	–
	mekal	0.30	1×10^{-6}	0.026	–	–	–
NGC 4449	apec	0.30	1×10^{-6}	0.060	–	–	–
	mekal	0.29	1×10^{-6}	0.060	–	–	–
NGC 5253	apec	0.73	9.7×10^{-5}	0.23	0.19	2.7×10^{-4}	0.40
	mekal	0.67	1.0×10^{-4}	0.094	0.19	3.5×10^{-4}	0.24

Plasma temperatures, normalizations, and intrinsic absorbing columns found in X-ray spectral fitting.

Table 4.4 Diffuse soft X-ray source fluxes, energy fluxes, and luminosities

Galaxy	Source Fluxes (10^{-5} photons s^{-1} cm^{-2})		Energy Fluxes (10^{-14} ergs s^{-1} cm^{-2})		Luminosities (10^{38} ergs s^{-1})	
	apec	mekal	apec	mekal	apec	mekal
NGC 625	0.68 ± 0.09	0.62 ± 0.09	0.81 ± 0.11	0.72 ± 0.11	0.17 ± 0.02	0.15 ± 0.02
NGC 1569	7.3 ± 0.6	6.8 ± 0.6	9.6 ± 0.8	8.9 ± 0.8	1.3 ± 0.1	1.2 ± 0.1
NGC 4214	8.5 ± 0.6	9.1 ± 0.6	8.7 ± 0.6	9.4 ± 0.6	0.91 ± 0.06	0.98 ± 0.06
NGC 4449	36 ± 1	39 ± 1	38 ± 1	41 ± 1	8.4 ± 0.2	9.1 ± 0.2
NGC 5253	7.8 ± 0.2	7.6 ± 0.2	8.7 ± 0.2	8.5 ± 0.2	1.3 ± 0.03	1.3 ± 0.03

Diffuse soft (0.35-1.0 keV) X-ray source fluxes, energy fluxes, and luminosities, calculated using the apec and mekal thermal plasma models.

Figure 4.1 DDO 165, NGC 625, NGC 1569 three-color X-ray images

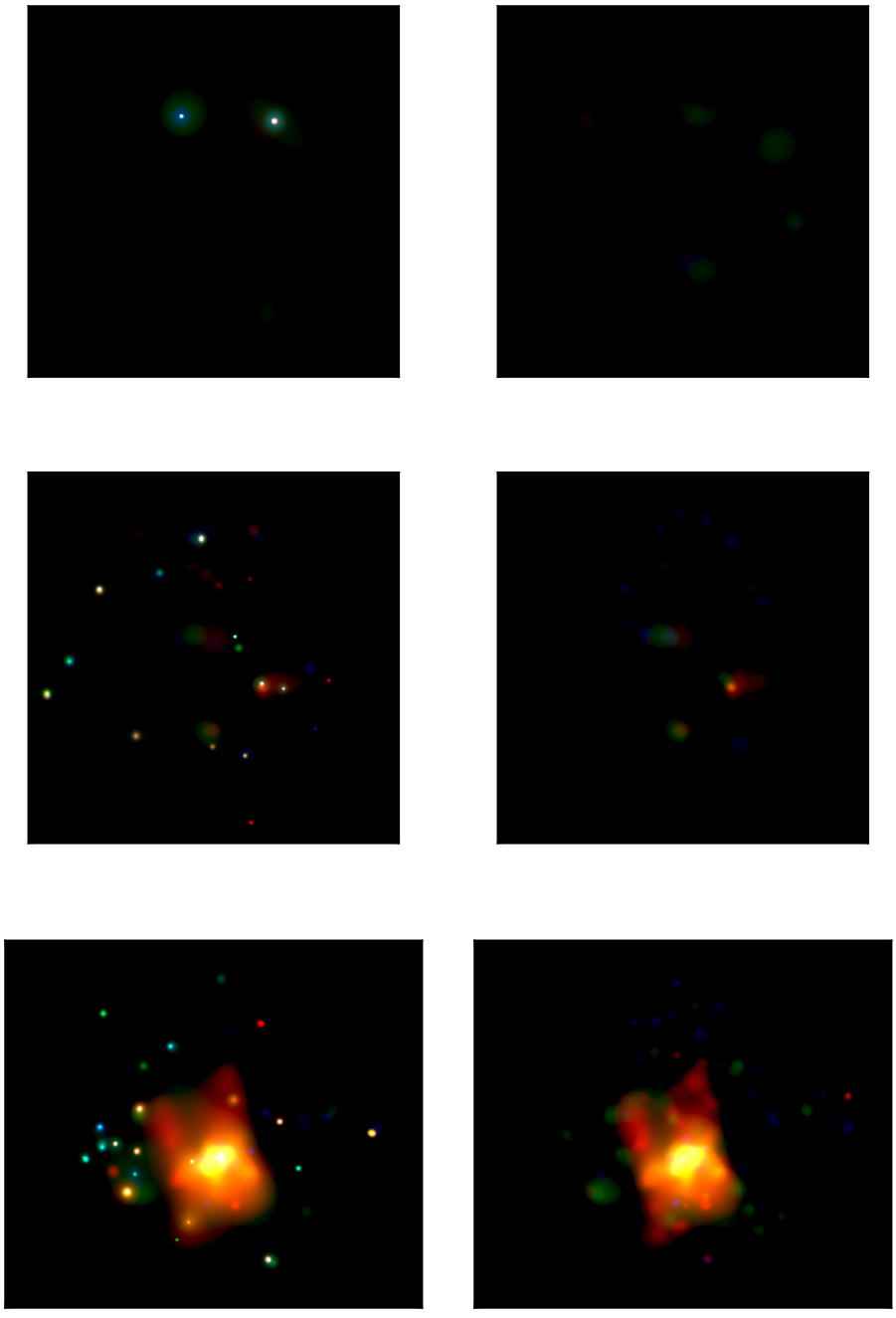

Left panels: Soft (red), medium (green), and hard (blue) *Chandra* X-ray emission with point sources in DDO 165, NGC 625, and NGC 1569 (top, center, and bottom rows, respectively). Right: The same combined images as in the left panel, with the point sources removed.

Figure 4.2 NGC 4214, NGC 4449, NGC 5253 three-color X-ray images

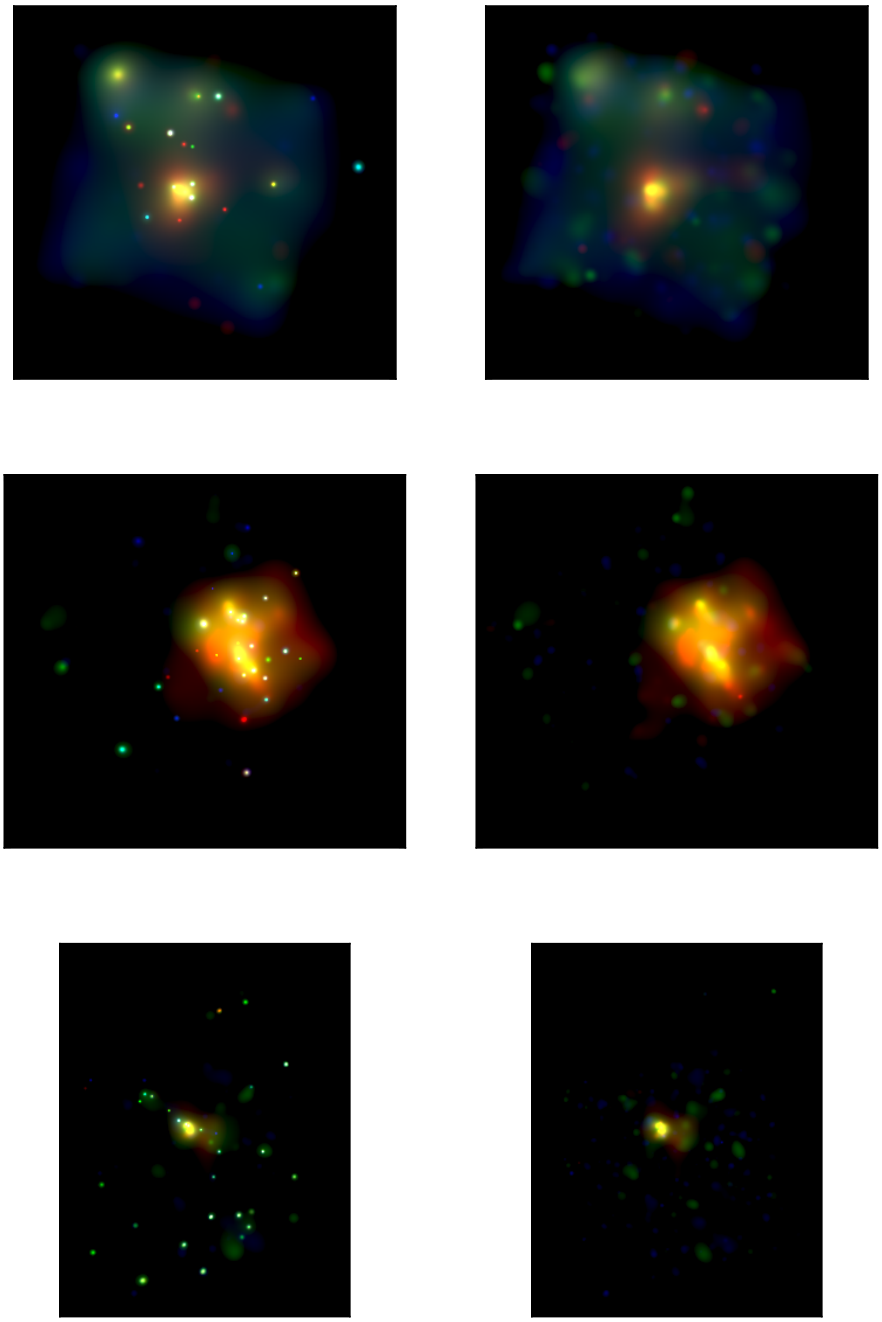

Left panels: Soft (red), medium (green), and hard (blue) *Chandra* X-ray emission with point sources in NGC 4214, NGC 4449, and NGC 5253 (top, center, and bottom rows, respectively). Right: The same combined images as in the left panel, with the point sources removed.

Chapter 5

Discussion

5.1 Morphology Comparison with H I, Optical, and NUV Images

Figures 5.1−5.6 show contours from the diffuse, soft x-ray emission overlaid on H I, R-band, and NUV images for each galaxy. In this section, the morphology of the diffuse X-ray emission is compared and contrasted with the imaging at other wavelengths.

DDO 165, shown in Figure 5.1, has only two contours at the 2σ level, neither of which is obviously associated with the galaxy or any optical counterpart. These could be unresolved background AGNs, or possible artifacts from the adaptive smoothing algorithm. The combined exposure times for DDO 165 were only 24 ksec, making this the shallowest observation in the sample by more than a factor of two. As there was no diffuse emission associated with the galaxy at the 2σ level, there was no emission boundary for spectral fitting, thus DDO 165 has been excluded from further analysis.

NGC 4214, shown in Figure 5.2, gives evidence of emission extended just beyond the optical disk, however, emission is contained well inside of the H I disc. At the 2σ level, emission extends furthest in the northeast direction, along the minor axis of the galaxy. The emission is asymmetric at this level, extending $\sim$ 4.5 arcmin or 3.4 kpc from the galactic center in the northeast, and only 3 arcmin or 2.2 kpc from the galactic center in the southwest. There are no obvious features in the radio, optical, or NUV images to explain this asymmetry. At the 4σ level, two "finger-like" features extend to

the west and northwest of the center of the galaxy, each spanning about 3 arcmin. The northwest finger is coincident with a clump of young stars, clearly visible in the NUV image, while the west pointing finger has no obvious optical counterpart. However, the western finger is associated with a clear underdensity in H I emission. This could be emission produced in the central regions of the galaxy that is escaping along the path of lowest gas density. There is also an X-ray emitting region north of the star forming disk at an 8σ level, however this feature is much less pronounced in an image smoothed with a fixed-sized Gaussian kernel, and is likely due to an unresolved background source that was not fully subtracted.

NGC 4449, shown in Figure 5.3, has emission extending well beyond the optical disk along major and minor axes of the galaxy. The hot gas approaches, but does not exceed the H I disc of the galaxy. With the exception of a fingerlike extension to the southeast, the emission is largely symmetric and extends $\sim$ 5 arcmin or 5.5 kpc in all directions. While there is no obvious feature in the optical, or NUV images associated with the southeast finger, the H Iemission shows an underdensity in that region. At the lower confidence levels, the emission is mostly symmetric, while at the 16, 32, and 64σ levels, asymmetries appear to be associated with bright star clusters seen in the optical and NUV images.

In Figure 5.4, NGC 1569 shows evidence extended emission along the minor axis of the galaxy, at very high (32σ) confidence levels. The extent of the X-ray emission exceeds both the optical and the H I disks, however they are entirely constrained to the minor axis, unlike NGC 4449. The lower confidence levels are largely symmetric and small features show no obvious counterparts in optical or NUV. The extent of the gas is $\sim 4.8 \times 3.2$ arcmin, corresponding to 3.1 x 2 kpc. At the 32σ level, there is a finger-like asymmetry in the northeast direction that has no obvious associated feature at any of the ancillary wavelengths. The 64σ level is contained within the galaxy along the northern axis, but extends outside of the star-forming disk towards the southern axis. The H I image shows a lower density along the southern edge, showing another anti-correlation between X-ray and H I emission. Additionally, the H I disk is extended further in the western direction along the major axis, while the X-ray emission is contained further inwards along that axis.

In Figure 5.5, NGC 5253 shows a narrow finger of emission extending just beyond

the optical disk, ∼1.5 arcmin or 2.4 kpc from the center, in the south at a 2σ confidence level. Like NGC 4449, the X-ray emission for NGC 5253 approaches but does not extend beyond the edge of the H I disk. There is a smaller extension to the west, along the minor axis, that persists at the 4 and 8σ levels. Neither of these features have obvious correlations or anticorrelations at other wavelengths. At the lower confidence levels, emission is elongated along the minor axis while at higher confidence levels emission is mostly symmetric about the galactic center. NGC 5253 is fainter in the optical and NUV than the previous three galaxies, and also has much less extended X-ray emission.

NGC 625, shown in Figure 5.6, does not show evidence of extended emission. The X-rays are constrained well inside of both the optical and H I disks. The feature at the eastern edge of the optical disk is most likely a noise artifact from the adaptive smoothing algorithm, and not associated with the galaxy. Emission is centrally located and correlated with the stellar populations seen in the optical image. Lower confidence levels show an east-west asymmetry, which follows the stellar distribution along the major axis. The higher confidence levels are symmetric at the very center of the galaxy.

Figure 5.1 DDO 165 X-ray Morphology

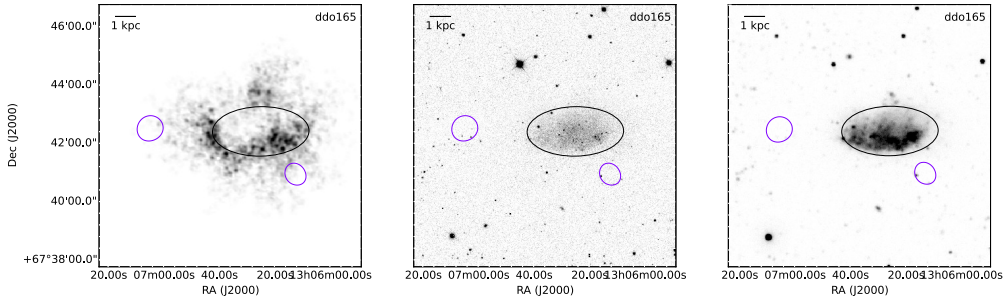

Images of DDO 165 (left: 21 cm neutral hydrogen emission map; center: DSS R-band optical image; right: GALEX NUV image), each overlaid with contours of soft X-ray emission corresponding to 2, 4, 8, 16, 32, and 64 σ. The black ellipses represent the main optical disk of the galaxy measured by the 25 m_B arcsec^{-2} isophote.

Figure 5.2 NGC 4214 X-ray Morphology

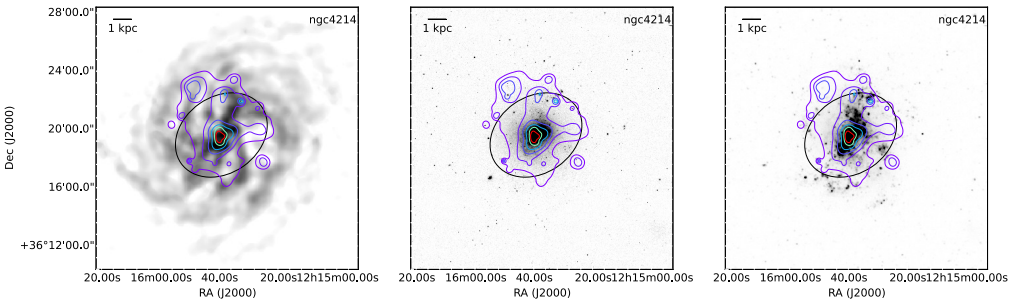

Images of NGC 4214 (left: 21 cm neutral hydrogen emission map; center: DSS R-band optical image; right: GALEX NUV image), each overlaid with contours of soft X-ray emission corresponding to 2, 4, 8, 16, 32, and 64 σ. The black ellipses represent the main optical disk of the galaxy measured by the 25 m_B arcsec^{-2} isophote.

5.2 X-ray Luminosity and Star Formation Histories

Figure 5.7 shows the observed soft band diffuse X-ray luminosities plotted against the stellar mass formed during the last 12.5, 25, 50, 100, 200, and 400 Myr of the starburst, as calculated in McQuinn et al. (2010b). We note that HST observational footprints for NGC 625 and NGC 4214 did not encompass the majority of their stellar disks. Therefore, the calculated stellar masses for these galaxies are presented as lower limits to the total star formation activity that could be contributing to creating an outflow or extended X-ray emission. Despite this limitation, X-ray luminosity shows a strong correlation with stellar mass formed during various timescales throughout the burst. Statistics for the line fits in this figure are displayed in Table 5.1. As the line fits were log-log, the R-value is not a straightforward measure, so goodness of fit is considered based on P-value (significance value of the correlation of X-ray emission to SFH at the varying timescales), and the standard error of the line fit.

With our small sample size, we cannot confidently quantify this relationship, however our findings do strongly suggest a relationship that would be a promising avenue for follow-up studies. The strongest correlation appears at the shortest, 12.5 Myr timescale, which is consistent with previous observations, e.g. Heckman et al. (1995); Martin et al. (2002), whose kinematic analysis is based on a starburst timescale of ∼10 Myr.

Figure 5.3 NGC 4449 X-ray Morphology

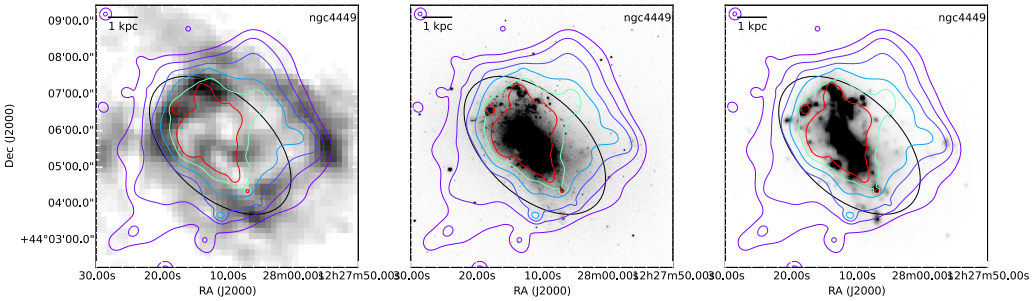

Images of NGC 4449 (left: 21 cm neutral hydrogen emission map; center: DSS R-band optical image; right: GALEX NUV image), each overlaid with contours of soft X-ray emission corresponding to 2, 4, 8, 16, 32, and 64 σ. The black ellipses represent the main optical disk of the galaxy measured by the 25 m_B arcsec^{-2} isophote.

Interestingly, the correlation significance drops in the intermediate timescales, but rises again at longer timescales. Further analysis on the full STARBIRDS sample would determine if this degeneracy is real, or an artifact of the sample.

The increased correlation to X-ray emission over longer timescales makes sense when juxtaposed with the time varying star formation histories from McQuinn et al. (2010b), which show that the peak star formation rates for these galaxies do not occur in recent times, with the exception of NGC 4449. While NGC 4449 is a simple case: it is both the most luminous X-ray galaxy and has the highest average and short timescale star formation rate, each by a factor of $\sim$3, a discrepancy appears when looking at NGC 1569 and NGC 5253. These galaxies are also bright in the X-ray, with approximately the same soft X-ray luminosity, but have very different star formation histories. NGC 1569 has made more stars recently, with the peak star formation rate occurring around 50 Myr ago, while NGC 5253 had a star formation peak 400-500 Myr ago and has declined ever since.

Figure 5.4 NGC 1569 X-ray Morphology

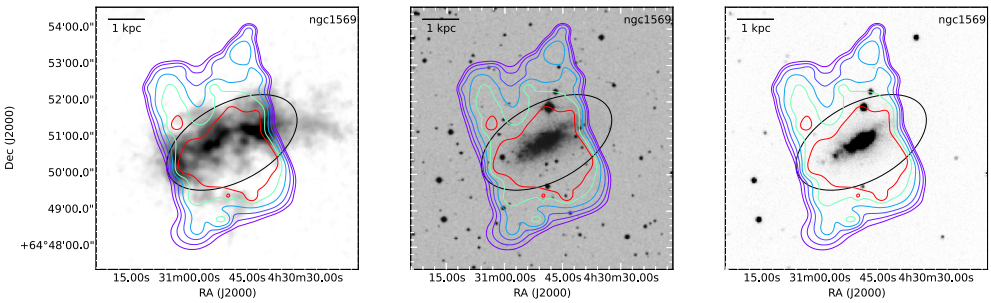

Images of NGC 1569 (left: 21 cm neutral hydrogen emission map; center: DSS R-band optical image; right: GALEX NUV image), each overlaid with contours of soft X-ray emission corresponding to 2, 4, 8, 16, 32, and 64 σ. The black ellipses represent the main optical disk of the galaxy measured by the 25 m_B arcsec^{-2} isophote.

5.3 X-ray Flux, UV Flux, and Timescales

Figures 5.8 shows the observed diffuse X-ray flux plotted against NUV and FUV flux contained within the optical disk of the galaxies, with statistics from the line fits displayed in Table 5.1. FUV emission corresponds to emission from stars formed in the last ∼100 Myr, while NUV emission corresponds to star formation over the last ∼200 Myr (Kennicutt & Evans, 2012). There is a clear correlation between the X-ray flux and both the FUV and NUV fluxes, with less scatter in the X-ray NUV relation. This adds significance to the stronger correlations at 200 and 400 Myr timescales compared to the intermediate scales in the previous section. These results suggest that diffuse X-ray emission may be a tracer the impact of star formation activity over longer timescales than previously studies have accounted for. Additionally, a planned avenue for future study will be to quantitatively compare the X-ray flux with Hα flux, which traces instantaneous (∼3 Myr) star formation timescales (Kennicutt & Evans, 2012), to further investigate the strong correlation on the short timescale end.

Burst timescales (McQuinn et al., 2010b, 810 Myr for NGC 4214, 450 Myr for the other galaxies), are ∼2 orders of magnitude longer than the time required for the superbubbles to propagate assuming expansion velocities of 200-400 km/s (e.g., NGC 4449, NGC 1569 Summers et al., 2003; Martin et al., 2002). Summers et al. (2003)

Figure 5.5 NGC 5253 X-ray Morphology

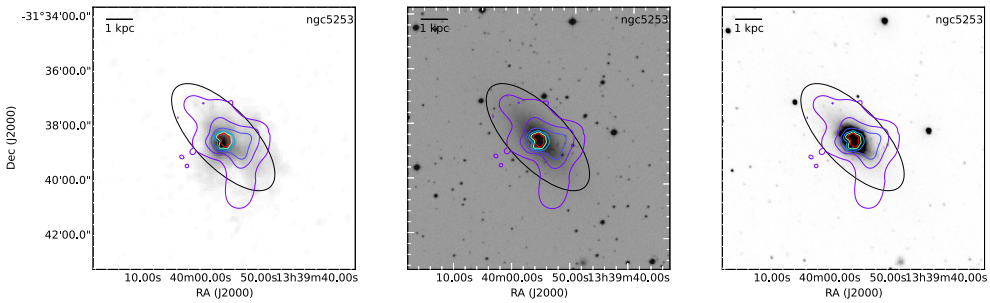

Images of NGC 5253 (left: 21 cm neutral hydrogen emission map; center: DSS R-band optical image; right: GALEX NUV image), each overlaid with contours of soft X-ray emission corresponding to 2, 4, 8, 16, 32, and 64 σ. The black ellipses represent the main optical disk of the galaxy measured by the 25 m_B arcsec^{-2} isophote.

calculated for NGC 4449, the most energetic galaxy in the sample, that with observed expansion velocities, it would take 200 Myr for bubbles to reach the edge of the 40 kpc halo. This is on the same order as the cooling time and suggests that the galaxy may retain most or all of the hot wind. Our SFH data gives a burst duration of 450 Myr for this galaxy, more than twice the calculated escape time for wind at these energies. This suggests that the X-ray bubbles may be much older than their dynamical timescale would suggest, and have been carved out over the duration of the burst.

Our data show peak SFRs at times ranging from 50-250 Myr ago, well beyond the length of starburst activity of ∼10 Myr assumed in previous starburst wind analysis, Heckman et al. (e.g., 1995); Martin et al. (e.g., 2002). The time varying SFH over timescales of ∼0.5 Gyr is complex and will be inadequately modeled with constant, short duration SFRs, or models using instantaneous mechanical luminosity, Mac Low & Ferrara (e.g. 1999). Furthermore, simulations (e.g. Suchkov et al., 1994) and observations (e.g Strickland et al., 2000) find that X-ray emission is produced by shocks formed in interacting regions between SN ejecta wind and the ambient ISM, rather than just the wind fluid by itself. Complex physics go into the production of diffuse X-ray emission, and therefore inferring dynamical information is even less straightforward than dynamical analysis would suggest.

Figure 5.6 NGC 625 X-ray Morphology

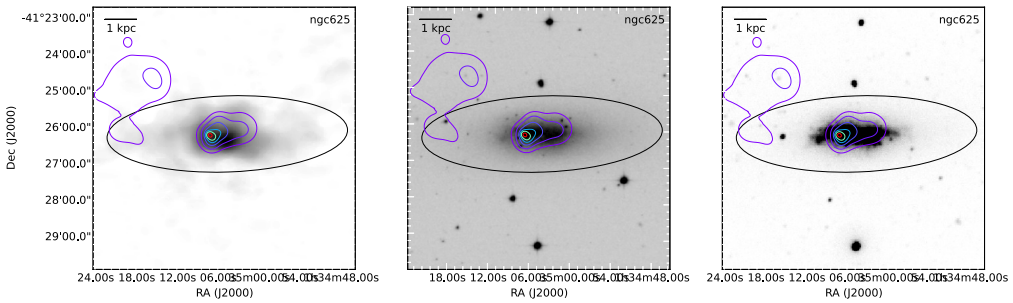

Images of NGC 625 (left: 21 cm neutral hydrogen emission map; center: DSS R-band optical image; right: GALEX NUV image), each overlaid with contours of soft X-ray emission corresponding to 2, 4, 8, 16, 32, and 64 σ. The black ellipses represent the main optical disk of the galaxy measured by the 25 m_B arcsec^{-2} isophote.

From morphological arguments, two galaxies, NGC 1569, and NGC 625, have straightforward conclusions. NGC 1569 has emission clearly extended beyond its H I halo, while NGC 625 is has emission entirely contained within the optical and H I disks. NGC 4214, NGC 4449, and NGC 5253 are more ambiguous. Their X-ray emission exceeds the optical disks and approaches or barely exceeds the H I disks. Given the long timescales associated with these starburst episodes compared to kinematic analysis, it suggest that the bubbles might be stalled, with models perhaps over-predicting the frequency of galactic outflows. Modeling with longer timescales and time varying star formation rates would give better insight as to whether the hot gas actually can escape the galaxies.

Table 5.1 X-ray emission compared to SFH and UV flux fit details

Star Formation Activity	R-value	P-value	Standard Error
12.5 Myr star formation	0.99	0.00035	0.064
25 Myr star formation	0.98	0.0024	0.10
50 Myr star formation	0.94	0.016	0.16
100 Myr star formation	0.92	0.026	0.17
200 Myr star formation	0.98	0.0035	0.092
400 Myr star formation	0.97	0.0056	0.10
FUV flux	0.90	0.040	0.16
NUV flux	0.99	0.0022	0.052

Goodness of fit parameters for diffuse X-ray luminosity and flux contrasted with stellar mass formed over various time intervals throughout the burst, and UV flux emitted within the optical disk.

Figure 5.7 X-ray luminosity compared to average SFR at varying timescales

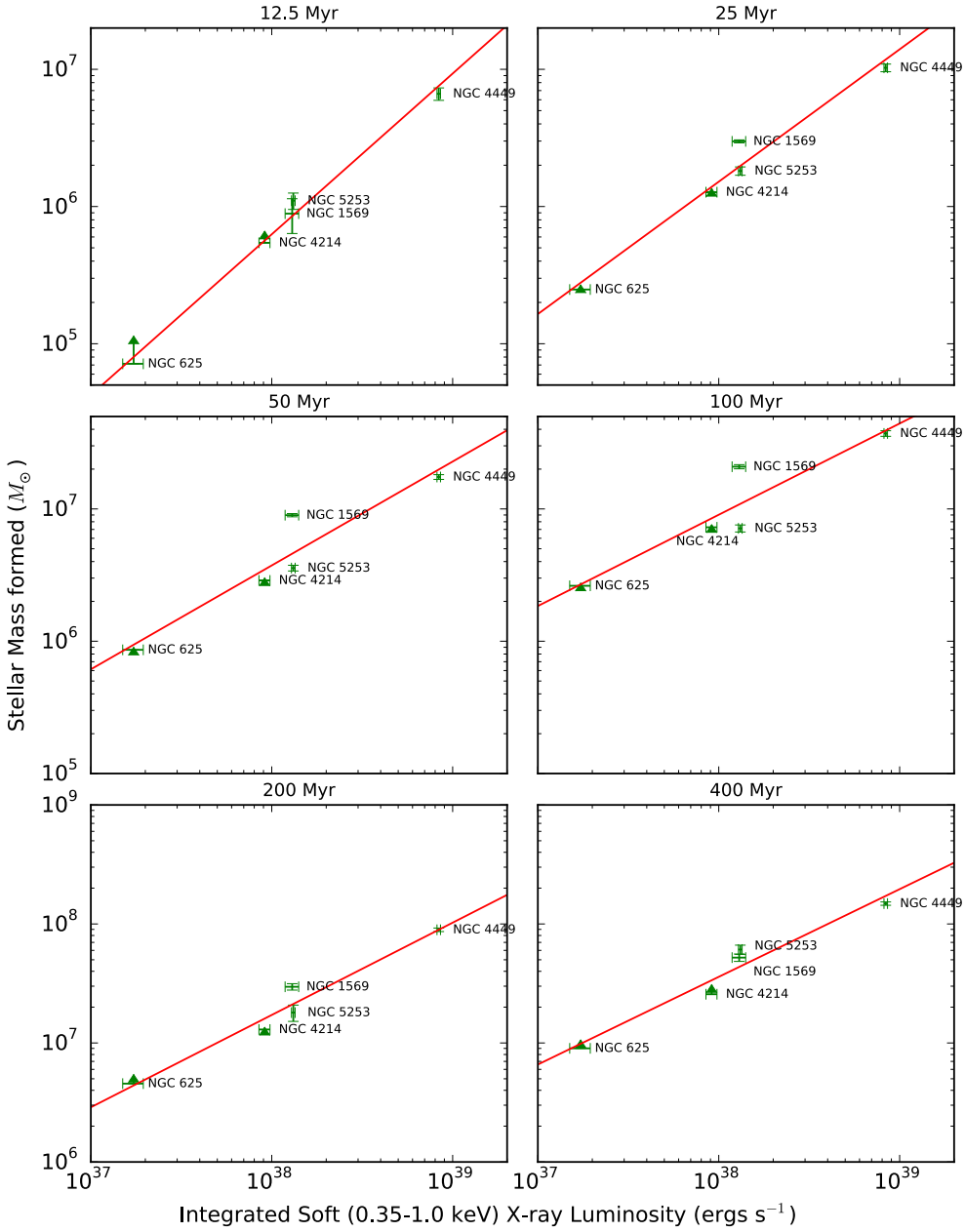

Soft X-ray luminosity plotted against stellar mass formed during the last 12.5 Myr (top left), 25 Myr (top right), 50 Myr (center left), 100 Myr (center right), 200 Myr (bottom left), and 400 Myr (bottom right).

Figure 5.8 X-ray flux compared to UV fluxes

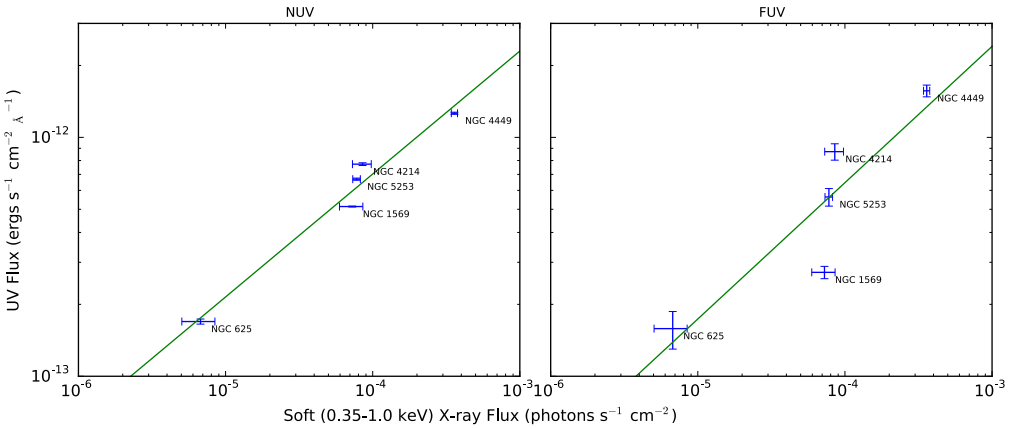

Left: Soft X-ray flux plotted against near UV flux contained inside the D_{25} isophote for each galaxy. Right: Soft X-ray flux plotted against far UV flux contained inside the D_{25} isophote for each galaxy.

Chapter 6

Conclusion

Diffuse X-ray emission is detected extending beyond the optical disk in 4 of 6 galaxies, however it is constrained within the H I haloes in all but NGC 1569. Diffuse X-ray luminosity correlates well with stellar mass formed at both very short and very long (12.5, 200-400 Myr timescales, respectively), but less strongly on middling timescales of 50-100 Myr. This result is additionally supported by comparing X-ray flux to NUV and FUV flux (200 and 100 Myr timescales, respectively), where the NUV is a significantly stronger correlation.

Future work with this sample will include comparing diffuse X-ray emission to Hα flux and possibly additional wavelengths from the STARBIRDS archive. Another avenue of exploration is to refine estimates of ejecta mass and kinetic energy, using methodology detailed in Martin et al. (2002) and our detailed SFHs from McQuinn et al. (2010b). This, combined with rough estimates of wind metallicity from X-ray spectral analysis could begin to quantify metal escape fraction as a function of X-ray luminosity and SFR. Those numbers, along with our results in this work, suggest that previous models considering only short, 10-20 Myr burst ages, constant star SFHs, and instantaneous stellar feedback are inadequate to model galactic winds. The next generation of starburst models will need to be more complex, with much longer timescales and time varying SFHs, to accurately model stellar feedback and galactic winds.

References

Alam, S., et al. 2015, arXiv:1501.00963v3

Asplund, M., Grevesse, N., Sauval, A. J., & Scott, P. 2009, ARA&A, 47, 481

Binder, B., Williams, B. F., Eracleous, M., et al. 2012, ApJ, 758, 15

Boch, T., & Fernique, P. 2014, Astronomical Data Analysis Software and Systems XXIII, 485, 277

Bonnarel, F., Fernique, P., Bienaymé, O., et al. 2000, A&AS, 143, 33

Broos, P. S., Townsley, L. K., Feigelson, E. D., Getman, K. V., Bauer, F. E., & Garmire, G. P. 2010, ApJ, 714, 1582

Broos, P. S., Townsley, L. K., Getman, K. V., Bauer, F. E. 2012, Astrophysics Source Code Library, 1203.001

Buat, V., Iglesias-Paramo, J., Seibert, M., et al. 2005, ApJ, 758, L51

Bykov, A. M., Paerels, F. B. S., & Petrosian, V. 2008, Space Sci. Rev., 134, 141

Cannon, J. M., Most, H. P., Skillman, E. D., et al. 2011, ApJ, 735, 35

Cen, R., & Chisari, N. E. 2011, ApJ, 731, 11

Dale, D. A., & Helou, G. 2002, ApJ, 576, 159

Dale, D. A., Cohen, S. A., Johnson, L. C., et al 2009, ApJ, 703, 517

Della Ceca, R., Griffiths, R. E., & Heckman, T. M. 1997, ApJ, 485, 581

de Vaucouleurs, G., de Vaucouleurs, A., Corwin, H. G., Jr., et al. 1991, Third Reference Catalogue of Bright Galaxies. Volume I: Explanations and references. Volume II: Data for galaxies between 0^h and 12^h. Volume III: Data for galaxies between 12^h and 24^h., by de Vaucouleurs, G.; de Vaucouleurs, A.; Corwin, H. G., Jr.; Buta, R. J.; Paturel, G.; Fouqué, P.. Springer, New York, NY (USA), 1991, 2091 p., ISBN 0-387-97552-7, Price US$198.00. ISBN 3-540-97552-7, Price DM 448.00. ISBN 0-387-97549-7 (Vol. I), ISBN 0-387-97550-0 (Vol. II), ISBN 0-387-97551-9 (Vol. III).

De Young, D. S., & Heckman, T. M. 1994, ApJ, 431, 598

Dolphin, A. E., 2002, MNRAS, 332, 91

Fitzpatrick, E. L. 1999, PASP, 111, 63

Ford, H. C., Bartko, F., Bely, P. Y., et al. 1998, Proc. SPIE, 3356, 234

Freeman, P., Doe, S., & Siemiginowska, A. 2001, Proc. SPIE, 4477, 76

Garmire, G. P., Bautz, M. W., Ford, P. G., Nousek, J. A., & Ricker, G. R., Jr. 2003, Proc. SPIE, 4851, 28

Girardi, L., Williams, B. F., Gilbert, K. M., et al. 2010, ApJ, 724, 1030

Grocholski, A. J., Aloisi, A., van der Marel, R. P., et al. 2008, ApJ, 686, L79

Gupta, A., Galeazzi, M., & Ursino, E. 2010, Bulletin of the American Astronomical Society, 41, #318.08

Hartwell, J. M., Stevens, I. R., Strickland, D. K., Heckman, T. M., & Summers, L. K. 2004, MNRAS, 348, 406

Heckman, T. M., Dahlem, M., Lehnert, M. D., et al. 1995, ApJ, 448, 98

Huchtmeier, W. K., Karachentsev, I. D., & Karachentseva, V. E. 2003, A&A, 401, 483

Holtzman, J. A., Hester, J. J., Casertano, S., et al. 1995, PASP, 107, 156

Jacobs, B. A., Rizzi, L., Tully, R. B., et al. 2009, AJ, 138, 332

Kennicutt, R. C., Jr., Armus, L., Bendo, G., et al. 2003, PASP, 115, 928

Kennicutt, R. C., & Evans, N. J. 2012, ARA&A, 50, 531

Koribalski, B. S., Staveley-Smith, L., Kilborn, V. A., et al. 2004, AJ, 128, 16

Lelli, F., Verheijen, M., & Fraternali, F. 2014, VizieR Online Data Catalog, 356, 60071

Mac Low, M.-M., & McCray, R. 1988, ApJ, 324, 776

Mac Low, M.-M., & Ferrara, A. 1999, ApJ, 513, 142

Makarov, D., Prugniel, P., Terekhova, N., Courtois, H., & Vauglin, I. 2014, A&A, 570, A13

Marigo, P., Girardi, L., Bressan, A., et al. 2008, A&A, 482, 883

Martin, C. L. 1998, Galactic Halos, 136, 141

Martin, C. L., Kobulnicky, H. A., & Heckman, T. M. 2002, ApJ, 574, 663

Martin, D. C., Fanson, J., Schiminovich, D., et al. 005, ApJ, 619, L1

Mas-Hesse, J. M., & Kunth, D. 1999, A&A, 349, 765

Matteucci, F., & Chiosi, C. 1983, A&A, 123, 121

McQuinn, K. B. W., Cannon, J. M., Dolphin, A. E., et al. 2014, ApJ, 785, 3

McQuinn, K. B. W., Mitchell, N. P., & Skillman, E. D. 2015, ApJS, 218, 29

McQuinn, K. B. W., Skillman, E. D., Cannon, J. M., et al. 2009, ApJ, 695, 561

McQuinn, K. B. W., Skillman, E. D., Cannon, J. M., et al. 2010, ApJ, 721, 297

McQuinn, K. B. W., Skillman, E. D., Cannon, J. M., et al. 2010, ApJ, 724, 49

McQuinn, K. B. W., Skillman, E. D., Dalcanton, J. J., et al. 2011, ApJ, 740, 48

McQuinn, K. B. W., Skillman, E. D., Dalcanton, J. J., et al. 2012, ApJ, 759, 77

McQuinn, K. B. W., Skillman, E. D., Dolphin, A. E., & Mitchell, N. P. 2015, ApJ, 808, 109

Mewe, R., Kaastra, J.S., & Liedahl, D.A., 1995, Legacy 6, 16

Morrissey, P., Schiminovich, D., Barlow, T. A., et al. 2005, ApJ, 619, L7

Morrissey, P., Conrow, T., Barlow, T. A., et al. 2007, ApJS, 173, 682

Mould, J., & Sakai, S. 2008, ApJ, 686, L75

Ochsenbein, F., Bauer, P., & Marcout, J. 2000, A&AS, 143, 23

Ott, J., Walter, F., & Brinks, E. 2005, MNRAS, 358, 1423

Raymond, J. C., & Smith, B. W. 1977, ApJS, 35, 419

Regan, M. W., & SINGS Team 2004, Bulletin of the American Astronomical Society, 36, 1443

Rieke, G. H., Young, E. T., Engelbracht, C. W., et al. 004, ApJS, 154, 25

Salpeter, E. E. 1955, ApJ, 121, 161

Schlafly, E. F., & Finkbeiner, D. P. 2011, ApJ, 737, 103

Schaerer, D., Contini, T., & Kunth, D. 1999, A&A, 341, 399

Searle, L., Sargent, W. L. W., & Bagnuolo, W. G. 1973, ApJ, 179, 427

Schlegel, D. J., Finkbeiner, D. P., & Davis, M. 1998, ApJ, 500, 525

Schnee, S., Bethell, T., & Goodman, A. 2006, ApJ, 640, L47

Schneider, S. E., Thuan, T. X., Mangum, J. G., & Miller, J. 1992, ApJS, 81, 5

Skillman, E. D. 1997, Revista Mexicana de Astronomia y Astrofisica Conference Series, 6, 36

Skillman, E. D., Côté, S., & Miller, B. W. 2003, AJ, 125, 593

Smith, R. K., Brickhouse, N. S., Liedahl, D. A., & Raymond, J. C. 2001, ApJ, 556, L91

Strickland, D. K., Heckman, T. M., Weaver, K. A., & Dahlem, M. 2000, AJ, 120, 2965

Suchkov, A. A., Balsara, D. S., Heckman, T. M., & Leitherer, C. 1994, ApJ, 430, 511

Summers, L. K., Stevens, I. R., Strickland, D. K., & Heckman, T. M. 2003, MNRAS, 342, 690

Summers, L. K., Stevens, I. R., Strickland, D. K., & Heckman, T. M. 004, MNRAS, 351, 1

Tüllmann, R., Gaetz, T. J., Plucinsky, P. P., et al. 011, ApJS, 193, 31